Characterization of dual-structure pore-size distribution of soil

X. Li and L.M. Zhang

Abstract: The microporosity structure of soil provides important information in understanding the shear strength, compressibility, water-retention ability, and hydraulic conductivity of soils. It is a soil characteristic that depends on sample preparation method and wetting–drying history. A comprehensive study of the microporosity structure of a lean clay with sand was conducted in this research to investigate variations of the microporosity structure during compaction, saturation, and drying processes. Scanning electron microscopy was used to observe the microporosity structure of soil sample surfaces. Mercury intrusion porosimetry was used to measure the microporosity structure quantitatively by showing the relationship between cumulative pore volumes and pore radius. The experimental results show that a dual-porosity structure (i.e., interaggregate pores and intra-aggregate pores) forms during the compaction process. The interaggregate pores are compressible and the associated volume is closely related to the final void ratio of the compacted sample. Changes to interaggregate pores is dominant during compaction, but changes to intra-aggregate pores is dominant during saturation and drying. Based on the experimental results, a dual-porosity structure model was developed by relating the pore-size distribution to the void ratio. Consequently, the pore-size distribution at any void ratio can be predicted.

Key words: compaction, pore-size distribution, soil fabric, dual porosity, compaction, saturation, drying.

Résumé : La structure de la microporosité des sols révèle des informations importantes pour la compréhension de la résistance au cisaillement, de la compressibilité, de la capacité de rétention d'eau et de la conductivité hydraulique des sols. La microporosité est une caractéristique du sol qui dépend de la méthode de préparation de l'échantillon ainsi que de son historique de saturation – drainage. L'étude présentée consiste en une investigation de la variation de la structure de la microporosité d'une argile avec sable durant sa compaction, saturation et drainage. Le microscope électronique à balayage a été utilisé pour observer la microporosité à la surface des échantillons. La porosimétrie par intrusion au mercure a évalué la structure de la microporosité quantitativement en démontrant la relation entre le volume cumulatif des pores et le rayon des pores. Les résultats expérimentaux montrent qu'une structure de porosité double (pores inter-agrégats et pores intra-agrégats) est formée durant le processus de compaction. Les pores inter-agrégats sont compressibles et leur volume est étroitement associé à l'indice des vides final du sol compacté. Les modifications aux pores inter-agrégats sont prédominantes durant le processus de compaction, tandis que les modifications aux pores intra-agrégats surviennent principalement durant la saturation et le drainage. Basé sur les résultats expérimentaux, un modèle de structure de porosité double a été développé en reliant la distribution de la dimension des pores et l'indice des vides. De cette façon, la distribution de la dimension des pores peut être prédite pour n'importe quel indice des vides.

Mots-clés : compaction, distribution de la dimension des pores, assemblage du sol, porosité double, saturation, séchage.

[Traduit par la Rédaction]

Introduction

The microporosity structure of a soil provides important information on the shear strength, compressibility, hydraulic conductivity, and soil–water characteristics of a soil. Soil microporosity structure is difficult to measure and is highly variable for a single soil type. Microporosity structure changes with stress state, transfer of water and air, temperature fluctuations, long-term gravimetric actions, and weathering.

During the past several decades, a number of studies have been undertaken on soil microporosity structure. Barden and Sides (1970) and Sridharan et al. (1971) studied interaggregate pores and intra-aggregate pores in compacted clays. This type of microporosity structure was called a "dual-structure" or "double-structure" by subsequent researchers (e.g., Alonso et al. 1987). Research studies showed that the interaggregate pores easily changed during soil compaction (Coulon and Bruand 1989; Penumadu and Dean 2000; Sivakumar and Wheeler 2000), consolidation (Delage and Lefebvre 1984; Griffiths and Joshi 1989), and drying (Simms and Yanful 2001; Cuisinier and Laloui 2004). The variations of interaggregate pores and intra-aggregate pores differed for different soils and under different conditions. The soil microporosity structure highly depended upon the soil preparation method and soil deformation history. Static compaction and vacuum saturation are widely used to prepare soil samples in the laboratory. A soil drying process involving several equilibrium suction values is also widely used for measuring the soil–water characteristic curves in the labora-

Received 17 April 2008. Accepted 11 October 2008. Published on the NRC Research Press Web site at cgj.nrc.ca on 6 February 2009.

X. Li and L.M. Zhang.[1] Department of Civil Engineering, Hong Kong University of Science and Technology, Clear Water Bay, Hong Kong.

[1]Corresponding author (e-mail: cezhangl@ust.hk).

Table 1. Experimental program.

Objective	Test No.	Void ratio at compaction	Void ratio at measurement	Sample preparation method	Experimental method
Investigation of microporosity structure formation due to compaction	C1	1.13	1.13	Compacted	MIP
	C2	1.05	1.05	Compacted	MIP
	C3	1.00	1.00	Compacted	MIP
	C4	0.76	0.76	Compacted	MIP
Investigation of microporosity structure after saturation	S5	1.17	1.17	Compacted and saturated	MIP
	S6	1.06	1.06	Compacted and saturated	MIP
	S7	0.91	0.91	Compacted and saturated	MIP
	S8	0.80	0.80	Compacted and saturated	MIP
Investigation of microporosity structure variation during drying process	S9	1.00	1.00	Compacted and saturated	MIP
	D10	1.00	0.96	Compacted, saturated, and drained to 100 kPa	MIP
	D11	1.00	0.84	Compacted, saturated, and drained to 500 kPa	MIP
	D12	1.00	0.65	Compacted, saturated, and oven-dried	MIP
Observation of microporosity structure on soil surfaces	C13	1.00	1.00	Compacted	SEM
	P14	—	—	Bulk, oven-dried	SEM
	S15	1.00	1.00	Compacted and saturated	SEM
	D16	1.00	0.65	Compacted, saturated, and oven-dried	SEM

tory. It is not clear how the soil microporosity structure forms and changes during the compaction, saturation, and drying processes. A comprehensive study is needed to quantitatively understand the formation and evolution of the soil microporosity structure during soil sample preparation, as well as the variations in soil microporosity structure during soil wetting–drying processes.

The objectives of this research are (*i*) to investigate the formation of a microporosity structure during compaction, the evolution of the microporosity structure after saturation, and the variation of the microporosity structure during the drying process both quantitatively and qualitatively; and (*ii*) to describe the pore-size distributions of soil samples at different states mathematically.

In this research, a comprehensive investigation of the microporosity structure was conducted on one lean clay with sand. Two techniques were used to study the soil microporosity structure; namely, scanning electron microscopy (SEM), used to characterize the soil surface structure directly, and mercury intrusion porosimetry (MIP), used to quantify the soil pore-size distribution (PSD). Based on the pore-size distribution curves obtained from the MIP tests, a mathematical model was developed to relate variations in the soil microporosity structure due to soil compaction, saturation, and drying to its void ratio. The microporosity structure of a soil sample at any void ratio can be predicted using the proposed model. It should be mentioned that this study was conducted only on one type of soil.

Experimental program

The experimental program involved the quantitative investigation of the microporosity structure and the measurement of the soil pore-size distributions using MIP. Four unsaturated compacted samples at different void ratios were tested to study the soil microporosity structure formation due to compaction. Four saturated compacted samples at different void ratio values were tested to study the soil microporosity structure after saturation. Four additional saturated compacted samples at the same void ratio were dried to different degrees of saturation and tested to study the microporosity structure variation during the drying process. To qualitatively investigate the microporosity structure, the soil surface characteristics were also studied using SEM on a bulk soil sample, an unsaturated compacted sample, a saturated compacted sample, and an oven-dried saturated compacted sample. In total, 12 soil samples in three series were used for pore-size measurements and four soil samples were used for the surface characteristics study, as summarized in Table 1.

The soil used in this research was derived from a completely decomposed granitic soil that was taken from a construction site located at Beacon Hill, Hong Kong. The grain-size distribution (GSD) curve and the grain-size density function are shown in Fig. 1*a*. The standard Proctor compaction test was performed in accordance with British Standards Institution standard BS 1377 (BSI 1990) and the results show a maximum dry density of 1550 kg/m^3 and an optimum water content of 20.5%. The liquid limit, plastic limit, and shrinkage limit of this soil are 47%, 32%, and 8%, respectively. The specific gravity is 2.64. The soil is classified as lean clay with sand (CL) according to ASTM D2487 (ASTM 2000). The soil–water characteristic curve (SWCC) of this soil at a dry density of 1320 kg/m^3 was measured in the laboratory using an axis-translation technique and is shown in Fig. 1*b*.

Fig. 1. Properties of the lean clay with sand used in this research: (*a*) grain size distribution; (*b*) drying soil–water characteristic curve.

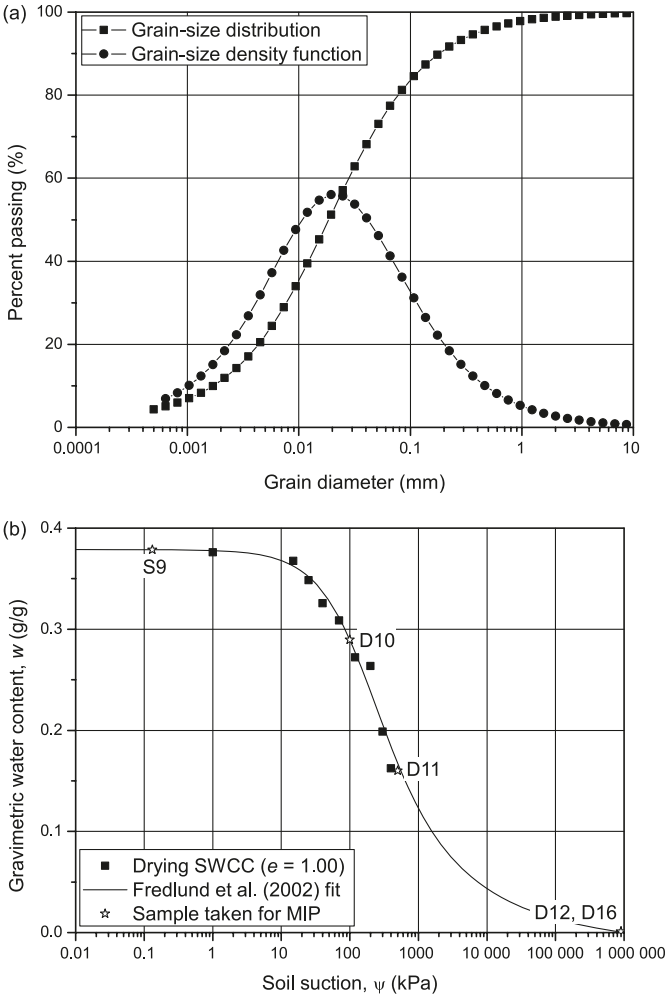

The unsaturated compacted samples were prepared in several steps. First, the soil was oven-dried in the laboratory. Then, the dry soil was mixed with water corresponding to the optimum water content. Many large soil lumps formed and the mixed soil was sieved through a 2 mm sieve to break up the large soil lumps. The mixed soil was subsequently stored in a plastic bag for 7 days for moisture homogenization. The water content of the soil was measured as 20.5%. The matured soil was statically compacted to a specified dry density value at a rate of 0.05 mm/min. Each soil sample was compacted inside a metal mold 70 mm in diameter and 20 mm in height. The compaction was performed in two layers. Scratches were made on the soil between layers to avoid segregation.

Eight compacted samples were saturated for 10 days in a mold subject to vacuum conditions, as shown in Fig. 2*a*. Five of these samples, with different void ratios, were tested using MIP directly (referring to Table 1) and three of them were subjected to various applied suction values (i.e., the difference between the pore-air pressure and the pore-water pressure). After the soil specimens were at equilibrium at a suction of 100 kPa (i.e., test D10 as shown in Table 1 and Fig. 1*b*), one soil specimen was taken from the SWCC device and used for MIP testing. The remaining soil specimens were further drained by applying a suction of 500 kPa (i.e., test D11 as shown in Table 1 and Fig. 1*b*). Then one specimen was used for MIP testing, and another specimen was oven-dried and used for MIP and SEM testing (i.e., tests D12 and D16 as shown in Table 1 and Fig. 1*b*).

Fig. 2. Experimental devices: (*a*) vacuum chamber for soil saturation; (*b*) freezing dryer; (*c*) JSM-6300 scanning electron microscope; (*d*) Micromeritics AutoPore IV 9500 V1.04 device.

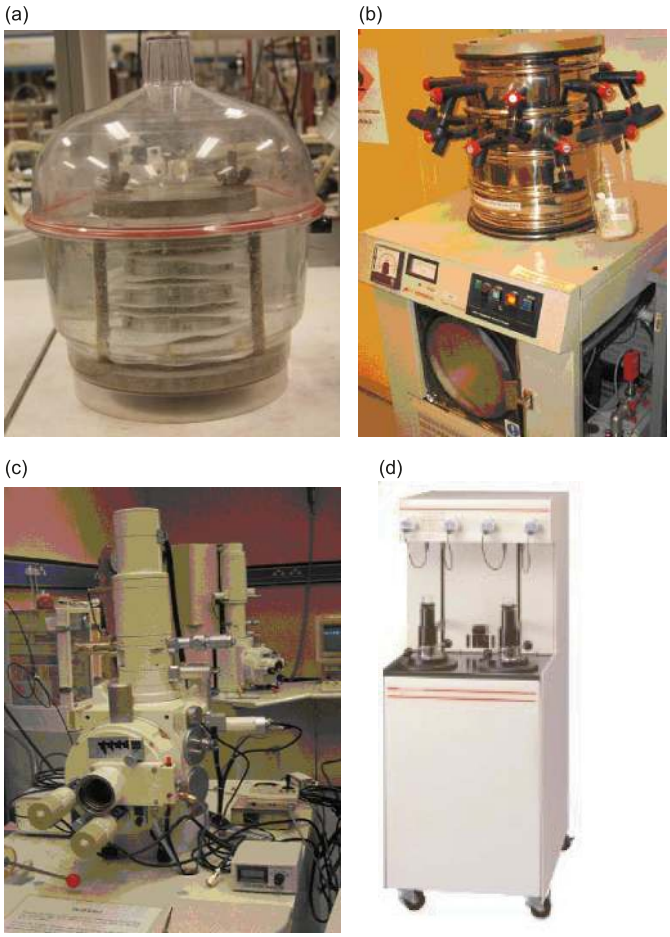

Experimental devices and techniques

The freeze-drying technique was used to dehydrate the wet soil samples for the MIP and SEM tests as it ie apparently the most appropriate method for dehydrating soil samples for use in microscopy and mercury intrusion testing (Penumadu and Dean 2000). The freeze-drying technique is based on the assumption that during rapid freezing of a soil using liquid nitrogen, the water in the soil does not have enough time to recrystallize. Therefore, the water passes directly to the solid state. The transition from liquid to a solid is not accompanied by a linear expansion of the phase being formed and consequently does not cause deformation to the specimen (Penumadu and Dean 2000). After freezing, the specimen is placed in a freezing unit with a vacuum chamber and dried by sublimation of the frozen water at a low temperature (e.g., lower than –20 °C). The freeze-drier used in this research was the Edwards Super Modulyo apparatus (Fig. 2*b*) and the freezing temperature was –40 °C.

SEM tests were used to observe the soil surface. The dehydrated soil specimens used in the SEM tests were coated with gold before taking the SEM images. A JSM-6300 scanning electron microscope, as shown in Fig. 2*c*, was used in this study. The macro–micro fabric at the soil surface can be recognized from the backscattered electron scanning images.

MIP tests are routinely and effectively used to evaluate the PSDs of powder and bulk materials with open and interconnected pore structures. MIP tests allow the measurement of pore radii ranging from a few nanometers up to several tens of micrometers. This wide range allows the identification of different soil pore classes along the PSD curve. MIP is based on the principle that a nonwetting fluid, such as mercury, does not enter a porous medium unless sufficient pressure is applied. During the MIP test, a dehydrated sample is initially surrounded with mercury at a specific low pressure. Then the mercury pressure is increased step by step until it reaches the capacity of the system. The volume of mercury that intrudes into the pores is measured for each pressure increment. The MIP apparatus used in this study was the Micromeritics AutoPore IV 9500 V 1.04 MIP device as shown in Fig. 2*d*, with a maximum intrusion pressure of 210 MPa.

An assumption is made that cylindrical flow channelswith a radius r exist in the soil, and the radius of the pores that are intruded by mercury under an applied pressure, P, can be calculated using Jurin's equation:

$$[1] \qquad r = \frac{2T_s \cos\alpha}{P}$$

where T_s is the surface tension of the fluid (i.e., mercury) and α is the contact angle of the fluid–air interface to the solid (i.e., soil particles). The T_s of mercury is 472 μm/m^2 at 20 °C . The contact angle is taken as 135° in this study.

The cumulative injected mercury volume indicates the cumulative pore volume. The mercury intrusion pressure indicates the pore radius according to eq. [1]. The pore-size distribution, $f(r)$, can be derived from:

$$[2] \qquad f(r) = \frac{\mathrm{d}v(r)}{\mathrm{d}r}$$

where r is the pore radius and $v(r)$ is the volume of pores with radii larger than r in 1 g of dry soil. When the pore radius approaches zero, $v(r)$ will be

$$[3] \qquad \lim_{r\to 0} v(r) = e/G_s$$

where e is the void ratio and G_s is the specific gravity.

Mathematical description of bimodal pore-size distribution

Bimodal pore-size distributions are characteristic of compacted soils (Alonso et al. 1987). Bimodal pore-size distributions are also frequently observed in structured soils, such as undisturbed aggregated loams (Mallants et al. 1997), residual soils (Rao and Revanasiddappa 2005), and sediments (Anandarajah and Lavoie 2002). Some porous media, such as fractured rocks and cracked soils, that exhibit significant secondary structures also have a bimodal pore-size distribution (Pruess et al. 1990; Zhang and Fredlund 2003).

Fig. 3. Pore-size distribution of a compacted soil sample.

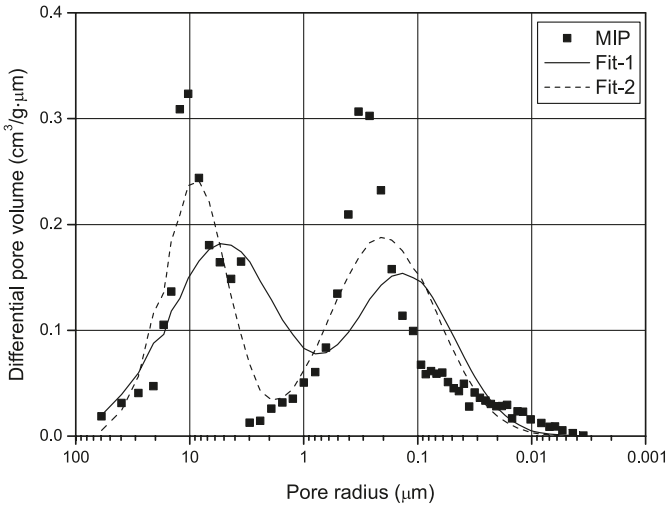

The pore-size distribution of one compacted soil specimen tested in this study is shown in Fig. 3. The curve exhibits a bimodal nature with one peak occurring at a pore radius of 10 μm and another peak occurring at 0.3 μm. Mathematically, a bimodal PSD, $f_B(r)$, can be obtained using the superposition of two overlapping unimodal pore-size distributions, (e.g., $f_1(r)$ and $f_2(r)$):

$$[4] \qquad f_B(r) = f_1(r) + f_2(r)$$

An appropriate mathematical equation needs to be obtained that best fits the soil data. The selection of an appropriate mathematical equation involves a review of a variety of equations that can be used to fit soil data (Fredlund et al. 2000). Fredlund et al. (2000) generated an equation that fits the unimodal grain size distribution quite well. The equation can also be used to characterize the unimodal pore-size distribution and to predict the SWCC (Fredlund et al. 2002). However, the equation is complex. In this paper, $f_1(r)$ and $f_2(r)$ are taken as simple log-normal functions. The bimodal pore-size distribution can be written as

$$[5] \qquad f_B(r) = a_1 f_1(r) + a_2 f_2(r) = \frac{a_1}{\sqrt{2\pi}\sigma_1 r} e^{-[(\log r - \mu_1)^2]/2\sigma_1^2} + \frac{a_2}{\sqrt{2\pi}\sigma_2 r} e^{-[(\log r - \mu_2)^2]/2\sigma_2^2}$$

where a_1 and a_2 are the parameters indicating the porosity values covered by distributions, $f_1(r)$ and $f_2(r)$, respectively; μ_1 and μ_2 are the corresponding mean radius values on a logarithmic scale; and σ_1 and σ_2 are the corresponding standard deviations on a logarithmic scale, respectively. The parameters a_1 and a_2, and the parameters defining $f_1(r)$ and $f_2(r)$, can be obtained by solving a set of moment equations:

$$[6] \qquad \int r^i f_B(r)\,\mathrm{d}r = \int a_1 r^i f_1(r)\,\mathrm{d}r + \int a_2 r^i f_2(r)\,\mathrm{d}r \qquad (i = 0, 1, 2, \ldots, n)$$

where n is equal to the number of the undetermined parameters minus 1.

The bimodal pore-size distribution can be artificially divided into two unimodal parts. Then a regression analysis can be applied to each unimodal part. The parameters can be obtained by solving,

$$[7]\quad \begin{cases} \displaystyle\int_R^{\infty} r^i f_B(r)\,dr = a_1 \int r^i f_1(r)\,dr \qquad (i = 0, 1, 2, \ldots, n_1) \\ \displaystyle\int_0^{R} r^i f_B(r)\,dr = a_2 \int r^i f_2(r)\,dr \qquad (i = 0, 1, 2, \ldots, n_2) \end{cases}$$

where R is the boundary pore radius that is chosen to artificially split the bimodal PSD into two parts; namely, $f_1(r)$, the normalized continuous distribution for describing the interaggregate pores (i.e., larger than R); $f_2(r)$, the normalized continuous distribution for describing the intra-aggregate pores (i.e., smaller than R). Variables n_1 and n_2 are the numbers of parameters used to define $f_1(r)$ and $f_2(r)$ minus 1.

Six parameters need to be determined in the regression analysis for a bimodal pore-size distribution. Transforming the log-normal distribution into a normal distribution by using $x = \log r$ as an independent variable, eq. [6] can be rewritten as (Lennart and Bertil 2004),

$$[8]\quad \begin{cases} \displaystyle\int f(x)\,dx = a_1 + a_2 \\ \displaystyle\int xf(x)\,dx = a_1\mu_1 + a_2\mu_2 \\ \displaystyle\int x^2 f(x)\,dx = a_1(\mu_1^2 + \sigma_1^2) + a_2(\mu_2^2 + \sigma_2^2) \\ \displaystyle\int x^3 f(x)\,dx = a_1\mu_1(\mu_1^2 + 3\sigma_1^2) + a_2\mu_2(\mu_2^2 + 3\sigma_2^2) \\ \displaystyle\int x^4 f(x)\,dx = a_1(\mu_1^4 + 6\mu_1^2\sigma_1^2 + 3\sigma_1^4) + a_2(\mu_2^4 + 6\mu_2^2\sigma_2^2 + 3\sigma_2^4) \\ \displaystyle\int x^5 f(x)\,dx = a_1\mu_1(\mu_1^4 + 6\mu_1^2\sigma_1^2 + 3\sigma_1^4 + 4\mu_1^2 + 12\sigma_1^2) + a_2\mu_2(\mu_2^4 + 6\mu_2^2\sigma_2^2 + 3\sigma_2^4 + 4\mu_2^2 + 12\sigma_2^2) \end{cases}$$

If the bimodal pore-size distribution is divided into two unimodal parts, $f_1(x)$ and $f_2(x)$, with a boundary pore radius of R, eq. [7] will be

$$[9]\quad \begin{cases} \displaystyle\int_{\log R}^{\infty} f(x)\,dx = a_1 \\ \displaystyle\int_{\log R}^{\infty} xf(x)\,dx = a_1\mu_1 \\ \displaystyle\int_{\log R}^{\infty} x^2 f(x)\,dx = a_1(\mu_1^2 + \sigma_1^2) \\ \displaystyle\int_{-\infty}^{\log R} f(x)\,dx = a_2 \\ \displaystyle\int_{-\infty}^{\log R} xf(x)\,dx = a_2\mu_2 \\ \displaystyle\int_{-\infty}^{\log R} x^2 f(x)\,dx = a_2(\mu_2^2 + \sigma_2^2) \end{cases}$$

As an example, if two log-normal distributions are used to simulate the PSD shown in Fig. 3, the solution to eq. [8] gives six parameters: $a_1 = 0.22$, $\mu_1 = 0.66$, $\sigma_1 = 0.49$, $a_2 = 0.17$, $\mu_2 = -0.91$, and $\sigma_2 = 0.43$. The results are plotted as curve "Fit-1" in Fig. 3. If the bimodal pore-size distribution is divided into two parts with a boundary pore radius equal to 2 μm and each part is simulated by a log-normal distribution, eq. [9] gives $a_1 = 0.17$, $\mu_1 = 0.92$, $\sigma_1 = 0.27$, $a_2 = 0.22$, $\mu_2 = -0.72$, and $\sigma_2 = 0.48$. The results are plotted as curve "Fit-2" in Fig. 3. The fitted cumulative pore volume curves are shown in Fig. 4. Figures 3 and 4 show that a better simulation is obtained when using "Fit-2".

Dual-porosity structure formation during soil compaction

Dual-porosity structure of compacted soil

Figure 5*a* shows the backscattered electron scanning image of one soil sample compacted at a water content of 20.5%. The void ratio of this soil sample was 1.00 and the corresponding dry density was 1317.5 kg/m^3. A dual-structure soil having both intra-aggregate pores and interaggregate pores can be seen in Fig. 5*a*. In Fig. 5*a*, the representative radius of the interaggregate pores is about 3 μm, and the representative radius of the intra-aggregate pores is about 0.6 μm.

For comparison purposes, the backscattered electron scanning image of the dry bulky soil sample is shown in Fig. 5*b*. The aggregates in the sample form a loose, uniform microporosity structure. The pores in the dry bulky soil are more uniform compared with those in the compacted sample and have a typical pore radius around 1 μm. Thin leafy edges are present around the soil aggregates in the dry bulk sample. In contrast, the edges around the soil aggregates are thicker in the compacted sample. The difference may be due to one of two main reasons. First, when mixing the soil particles and water, large soil aggregates form and appear to be associated with the water meniscus forces. Second, the compression stresses can reach 1200 kPa when producing a

Fig. 4. Cumulative pore volume curves from two fitting methods.

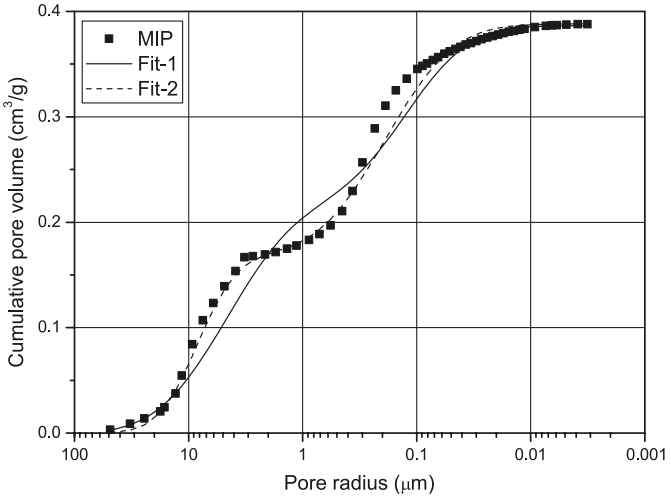

soil sample with a void ratio of 0.76 during the compaction process. The volumetric deformation of the bulk soil can reach 30% of the initial total volume and the total pore volume in the bulk soil decreases to 50% of its original value after it is compacted to a void ratio of 0.76. The distance between aggregates decreases because of the compression stresses and the stiff aggregates form a strong skeleton to carry the compression force and form large interaggregate pores. The distance between aggregates becomes closer as the compression stress is increased and some aggregates are believed to break and merge with others during the compaction process. Hence, the interaggregate pores become smaller and the number of interaggregate pores become fewer as the compression stress is increased.

Dual-porosity structure change due to soil compaction

The MIP technique was used to characterize the changes in the soil dual-structure due to compaction. Four soil samples were compacted to void ratios of 1.13, 1.05, 1.00, and 0.76, at optimum water content. The measured PSDs of the four samples are shown in Fig. 6*a*. The unsaturated compacted samples exhibit a distinct dual-porosity structure. In the intra-aggregate pore zone of the four distributions, the differential pore volume shows a peak at a radius of about 0.2 μm. The differential pore volumes of the four compacted samples are similar up to a radius of 2 μm. This is considered to be the boundary between the intra-aggregate pores and the interaggregate pores. In the interaggregate pore zone of the four compacted samples, the differential pore volumes show another peak at around 7–8 μm. The differential pore volumes with pore radii larger than 2 μm decrease sharply as the void ratio decreases. The pore volumes in 1 g of dry soil are compared in Fig. 7 with respect to pore radius. The pore volumes with radii smaller than 0.05 μm are similar in the four samples. The pore volumes with radii from 0.05 μm to 2 μm are also similar in the four samples. However, the pore volumes with radii larger than 2 μm (i.e., interaggregate pores) vary significantly, with a larger accumulated pore volume corresponding to a larger void ratio.

The measured pore-size distributions of the four compacted samples indicate that soil compaction changes the interaggregate structure of soil significantly, but only changes the intra-aggregate structure slightly up to a relative compaction value of 0.97 (e = 0.76). The total soil volume and void ratio became smaller and smaller as the compaction stress was increased. Simultaneously, the distance between aggregates became smaller as the compaction stress was increased. Therefore, the total volume of the interaggregate pores and the differential pore volume in the interaggregate pore zone of the differential curve became smaller and smaller as the compaction stress was increased. The compaction stress applied in this research may not be sufficiently high to change the intra-aggregate pores.

Two log-normal distribution curves were used to characterize these bimodal pore-size distributions. The parameters for the log-normal distribution curves are listed in Table 2. The fitted PSD curves are shown in Fig. 6*a*. The measured cumulative pore-volume curve and the cumulative pore-volume curves integrated from the fitted PSD curves are

Fig. 5. Scanning micrographs of samples: (*a*) unsaturated compacted soil sample, ×3500; (*b*) dry bulky soil sample, ×3700.

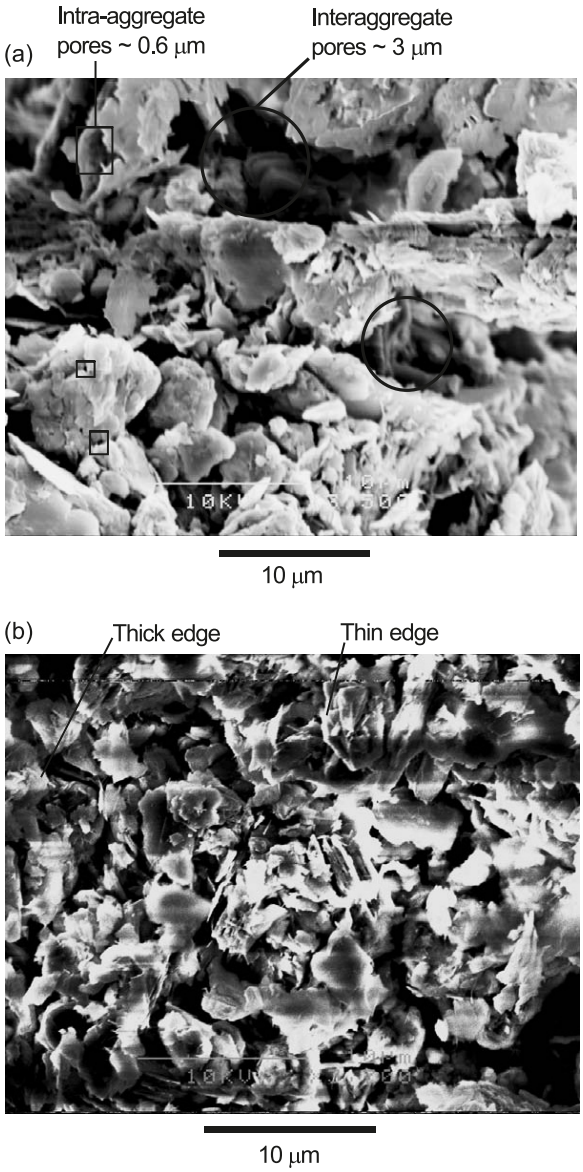

Fig. 6. Dual-porosity structure of unsaturated compacted samples: (*a*) differential pore-volume curves; (*b*) cumulative pore-volume curves.

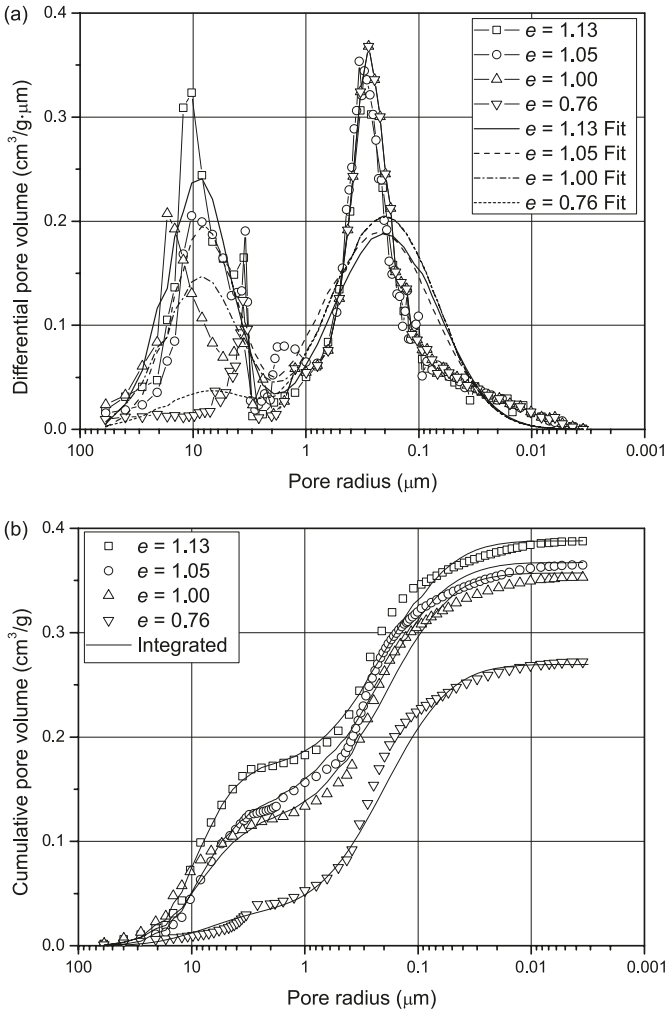

shown in Fig. 6*b*. The measured pore-volume curves and the integrated curves agree well.

Parameters a_1 and μ_1 shown in Table 2 indicate the porosity and log mean radius of the interaggregate pores. These values are shown to decrease significantly with the void ratio, whereas parameters a_2 and μ_2, which indicate that the porosity and log mean radius of the intra-aggregate pores, vary little with void ratio.

One noticeable phenomenon is that the sum of a_1 and a_2 is about 5% to 10% smaller than e/G_s (referring to eq. [3]). This difference occurs because there are some pores with radii outside the measurement range (i.e., from 0.003 to 60 μm for the Micromeritics AutoPore IV 9500). These pores cannot be measured and have not been included in the total pore volume.

Through regression analysis using the data in Table 2, parameter a_1, which indicates the pore volume with a radius larger than 2 μm, linearly increases with the void ratio (as shown in Fig. 8*a*). Parameter μ_1 also changes linearly with the void ratio (as shown in Fig. 8*b*). However, parameters a_2 and μ_2 show insignificant change with the void ratio.

Fig. 7. Variation of volumes of interaggregate pores and intra-aggregate pores in compacted samples.

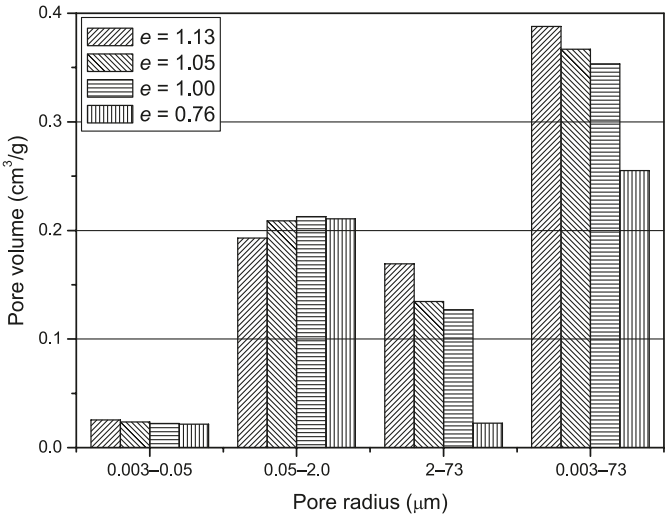

Formulation of dual-structure porosity change due to compaction

An attempt has been made to relate the pore-size distribution changes to changes in void ratio. Referring to eq. [5], the total soil volume change is the sum of the changes in the volumes of the interaggregate pores and the intra-aggregate pores:

$$[10] \qquad \Delta a_1 + \Delta a_2 = \frac{\Delta e}{G_s}$$

Introducing a parameter k_1, which indicates the percentage of interaggregate pore volume change over the total soil volume change, eq. [10] can be rewritten as

$$[11] \qquad \Delta a_1 = k_1 \frac{\Delta e}{G_s}$$

$$[12] \qquad \Delta a_2 = (1 - k_1) \frac{\Delta e}{G_s}$$

Changes in the mean logarithmic radii of interaggregate pores and intra-aggregate pores are considered to be linearly related to changes in void ratio

$$[13] \qquad \Delta \mu_1 = \lambda_1 \Delta e$$

$$[14] \qquad \Delta \mu_2 = \lambda_2 \Delta e$$

where λ_1 and λ_2 are empirical parameters.

The standard deviations, σ_1 and σ_2, indicate the shape of the interaggregate PSD and the shape of the intra-aggregate PSD, respectively. Assuming R is the boundary radius between the interaggregate pores and the intra-aggregate pores and only a certain percentage of the interaggregate pores is smaller than the boundary pore radius, then σ_1 is

$$[15] \qquad \sigma_1 = \lambda_3(\mu_1 - \log R)$$

where λ_3 is related to the specified percentage through the standard normal distribution function. If $\lambda_3 = 0.5$, eq. [14] can be transformed as $(\mu_1 - \log R)/\sigma_1 = 2$. That is to say,

Table 2. Best-fit analysis results for PSDs of samples compacted at optimum water content.

	PSD of interaggregate pores			PSD of intra-aggregate pores		
Void ratio	a_1 (cm^3/g)	μ_1	σ_1	a_2 (cm^3/g)	μ_2	σ_2
1.13	0.170	0.91	0.28	0.22	–0.74	0.46
1.05	0.130	0.87	0.28	0.23	–0.66	0.49
1.00	0.120	0.88	0.33	0.24	–0.72	0.46
0.76	0.035	0.84	0.38	0.24	–0.73	0.46

only 2.28% of interaggregate pores are smaller than R. If $\lambda_3 = 1$, then 15.87% of interaggregate pores are smaller than R. Similarly, assuming a certain percentage of the intra-aggregate pores is larger than the boundary pore radius,

$$[16] \qquad \sigma_2 = \lambda_4(\log R - \mu_2)$$

where λ_4 is, similar to λ_3, related to the specified percentage through the standard normal distribution function. The empirical parameters, k_1, λ_1, λ_2 λ_3, and λ_4, are calculated from the fitting parameters, a_1, a_2, μ_1, μ_2, σ_1, and σ_2, at different void ratios as shown in Fig. 8, and are considered to be dependent on soil type and soil state.

Parameters used to describe the PSDs of interaggregate pores and intra-aggregate pores can be related to the sample's void ratio through the application of eqs. [11]–[16]. Parameters k_1, λ_1, λ_2, λ_3, and λ_4 are all related to soil type and boundary conditions, and need to be calibrated to experimental data. The regression analysis based on the data in Table 2 gives $k_1 = 1$, $\lambda_1 = 0.17$, $\lambda_2 = 0$, $\lambda_3 = 0.6$, and $\lambda_4 = 0.5$. Note that $k_1 = 1$ indicates the soil volume change due to soil compaction in this study that is entirely based on compression of the interaggregate pores. After k_1, λ_1, λ_2, λ_3, and λ_4 have been determined, the pore-size distribution of a compacted sample at any void ratio can be predicted based on one known poresize distribution. The pore-size distributions at four different void ratios can be predicted and are shown in Fig. 9. As the fitted pore-size distributions in Fig. 6 are smoother than the measured curves and show lower peaks, the predicted pore-size distributions are also smoother than the measured curves shown in Fig. 6 and show lower peaks. This result indicates that the accuracy of prediction is highly related to the fitting curves used to calculate the empirical parameters (i.e., k_1, λ_1, λ_2, λ_3, and λ_4) and the equation used to fit the measured pore-size distributions. A better fitting equation can result in better fitting curves and better predictions.

The formulation for the dual-porosity structure of a compacted soil can be coupled with a model describing void ratio changes during soil compaction. For instance, if soil compaction is assessed using a linear relationship between void ratio e and the logarithm of the compression stress p, then eqs. [11]–[16] can be transformed by substituting p for e.

Dual-porosity structure evolution during soil saturation

The PSDs of five saturated compacted samples with different void ratios (i.e., 1.17, 1.06, 1.00, 0.91, and 0.80) were measured using the MIP technique and are shown in Fig. 10. These differential pore-volume curves indicate that the porosity of the saturated samples essentially consists of the intra-aggregate pores with a small fraction of interaggregate pores. In the intra-aggregate pore zone of these five saturated soil samples, the differential pore volumes show peaks at pore radii around 0.3–0.7 μm. The peak value and the pore radius at peak value are smaller for samples with lower void ratios among these five saturated samples. The pore volumes in 1 g of dry soil are compared in Fig. 11. The accumulated pore volumes in the interaggregate pore zone (i.e., pore radii larger than 2 μm) of the five saturated soil samples are no more than 8% of the total void volume.

The PSDs of one unsaturated and one saturated compacted sample at the same void ratio are compared in Fig. 12. Although the unsaturated compacted sample and saturated compacted sample have the same void ratios, their PSDs are quite different. Distinct bimodal PSD features can be seen for the unsaturated compacted sample, whereas only weak bimodal PSD features are present for the saturated compacted sample. In the intra-aggregate pore zone of the differential distributions (i.e., pore radii smaller than 2 μm), the pore radius at the peak value in the unsaturated com-

Fig. 8. Regression analysis of parameters indicating PSDs of samples compacted at optimum water content.

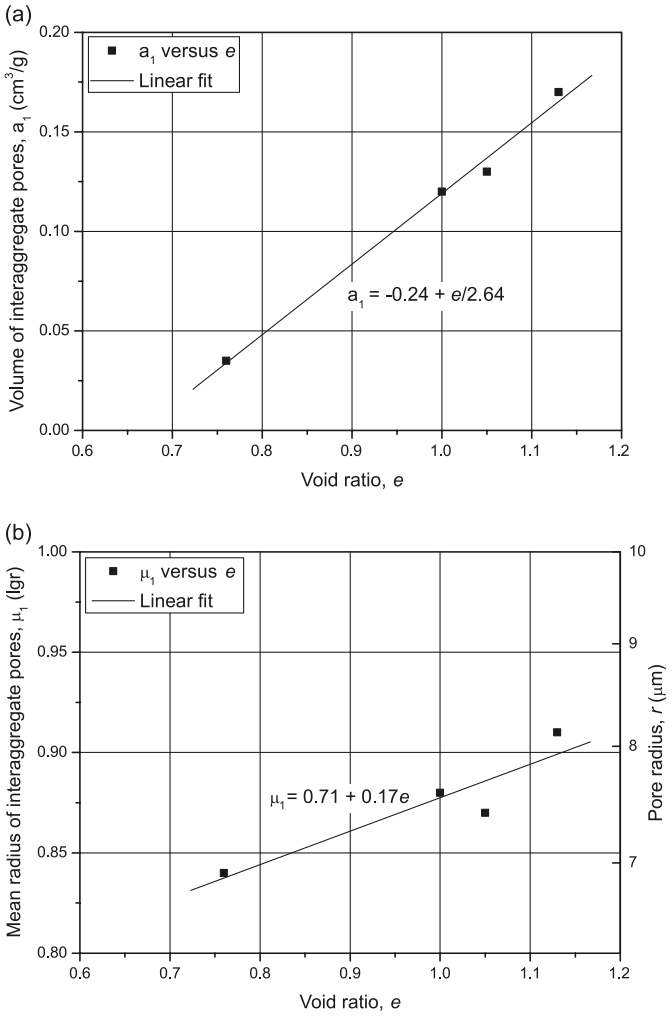

Fig. 9. Predicted PSDs of samples compacted at optimum water content with different void ratio values.

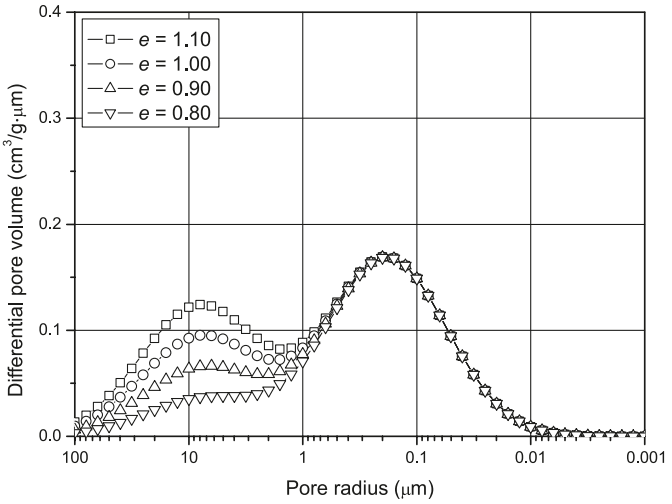

Fig. 10. Dual-porosity structure of saturated samples: (*a*) differential pore-volume curves; (*b*) cumulative pore-volume curves.

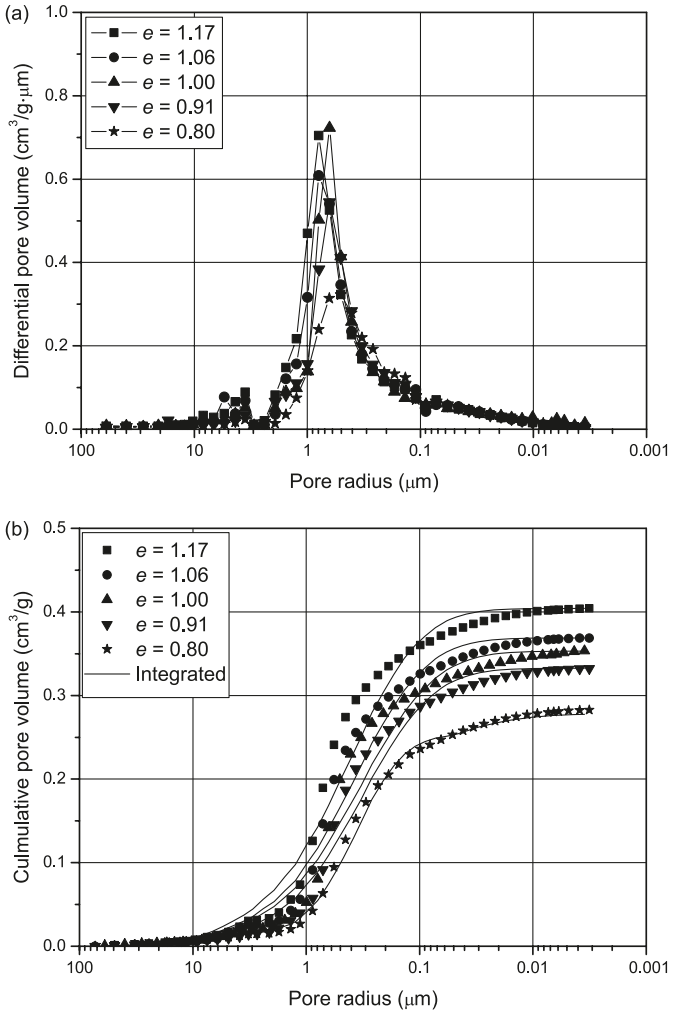

pacted soil sample is 0.27 μm, whereas the pore radius at the peak value in the saturated soil sample is 0.64 μm. The pore volumes in 1 g of dry solid of the compacted samples

Fig. 11. Variation of volumes of interaggregate pores and intraaggregate pores in saturated compacted samples.

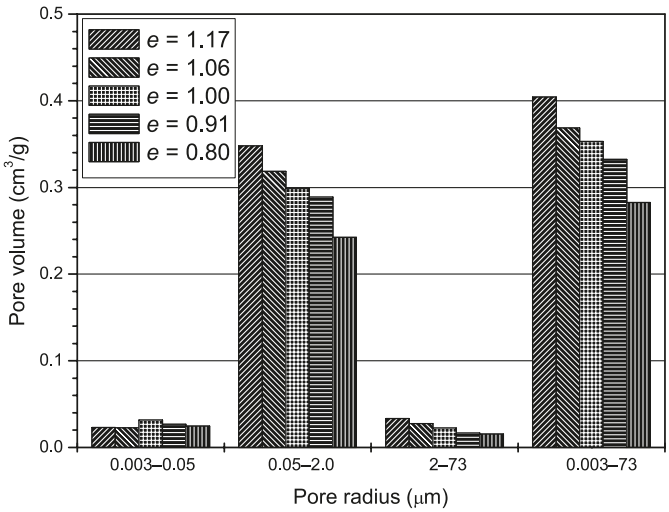

Fig. 12. Comparison of PSDs of saturated compacted sample and samples compacted at optimum water content and the same void ratio.

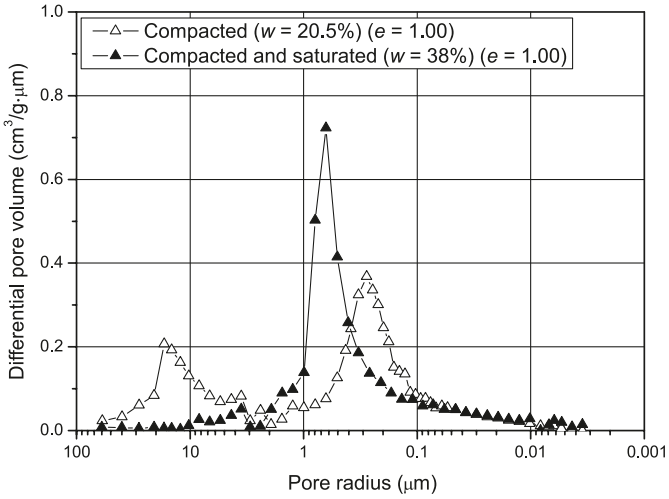

and saturated samples are compared in Fig. 13. In the intraaggregate pores zone, the accumulated pore volume in the compacted soil sample is smaller than that in the saturated soil sample. In the interaggregate pores zone, the accumulated pore volume in the compacted soil sample is much larger than that in the saturated soil sample.

The cyclic swelling and shrinkage of clays has been studied by numerous investigators (e.g., Basma et al. 1996). The lean clay with sand used in this study was sieved from completely decomposed granite. A mineral analysis by Zhao et al. (2005) showed that the fines of completely decomposed granite contained approximately 60% of kaolinite and 40% of ledikite. As the soil used in this research contains 80% fines and has a shrinkage limit of 8%, it is anticipated to swell upon wetting when its water content is larger than 8% (i.e., shrinkage limit). When the soil sample is being saturated under free boundary conditions, the soil sample will swell and the void ratio of the soil sample will increase. As part of the saturation method used in this study, the soil

Fig. 13. Comparison of the volumes of interaggregate pores and intra-aggregate pores in saturated compacted sample and samples compacted at optimum water content and the same void ratio.

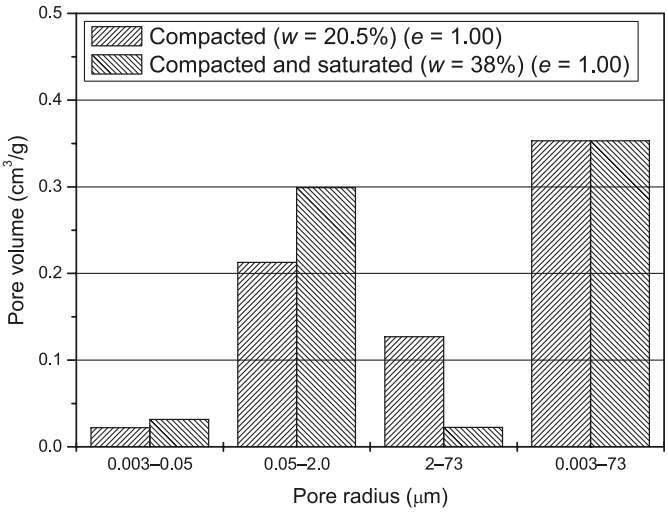

sample was placed inside a metal mold (Fig. 2*a*) and therefore, the total volume and void ratio of the soil sample could not change. As the soil aggregates swelled during the saturation process, the intra-aggregate pores became larger and the distances between soil aggregates became smaller because the sample was confined by the rigid mold. Consequently, the interaggregate pores became smaller as water content increased. The accumulated volume of interaggregate pores (i.e., the pores above 2 μm) decreased after saturation and the accumulated volume of intra-aggregate pores (i.e., the pores smaller than 2 μm) increased after soil saturation, as shown in Fig. 13. However, the total volume of soil remained approximately the same.

Formulations for dual-porosity structure of saturated soil samples

Two log-normal distributions were again combined to describe the pore-size distributions of the five saturated soil samples. One log-normal distribution was used to characterize the interaggregate pores (larger than 2 μm) and another was used to characterize the intra-aggregate pores with radii smaller than 2 μm. The parameters obtained from the regression analyses are listed in Table 3. The measured cumulative pore-volume curves and the integrated pore-volume curves based on the fitted PSDs are shown in Fig. 10*b*.

The interaggregate pore-size distributions and the intra-aggregate pore-size distributions are related to the void ratio through the application of eqs. [11]–[16]. Regression analyses were carried out based on the data listed in Table 3. The parameters obtained are $\lambda_1 = -0.54$, $\lambda_2 = 0.5$, $\lambda_3 = 0.9$, $\lambda_4 = 0.6$, and $k_1 = 0.75$. Note that $k_1 = 0.75$ means that about 75% of the volume change occurs in the intra-aggregate pores and only about 25% of the volume change occurs in the interaggregate pores for saturated soil samples. The pore-size distribution of a soil sample at any void ratio can be predicted based on its pore-size distribution associated with one void ratio (i.e., 1.17 in this case as shown in Fig. 10*a*). The pore-size distributions at four different void ratios are predicted and are shown in Fig. 14. Similar to the predictions for the compacted soil samples, the predicted pore-size distributions for the saturated soil samples are smoother than the measured pore-size distributions in Fig. 10 and show lower peaks.

Table 3. Best-fit analysis results for PSDs of saturated compacted samples.

	PSD of interaggregate pores			PSD of intra-aggregate pores		
Void ratio	a_1 (cm^3/g)	μ_1	σ_1	a_2 (cm^3/g)	μ_2	σ_2
1.17	0.040	0.67	0.36	0.36	–0.43	0.49
1.06	0.031	0.71	0.34	0.34	–0.47	0.49
1.00	0.027	0.74	0.41	0.33	–0.52	0.52
0.91	0.022	0.79	0.42	0.31	–0.53	0.49
0.8	0.017	0.87	0.40	0.27	–0.62	0.51

Fig. 14. Predicted pore-size distributions of saturated compacted samples with different void ratios.

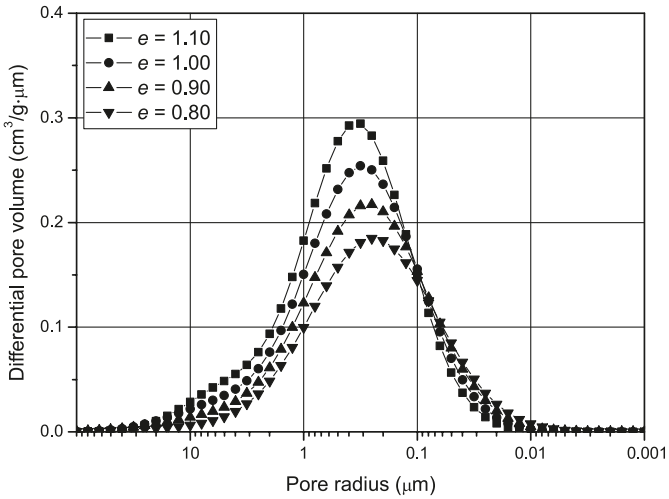

Dual-porosity structure change during drying process

Dual-porosity structure changes during drying

The backscattered electron scanning images of one saturated compacted sample and one compacted sample that was first saturated and then oven-dried are shown in Figs. 15*a* and 15*b*, respectively. The aggregates in the oven-dried sample are much closer and larger than those in the saturated sample. A dual-porosity structure similar to that of the unsaturated compacted sample shown in Fig. 5 can be found in the saturated soil sample (Fig. 15*a*). Some interaggregate pores with radii between 1 and 5 μm are present in the saturated soil sample, whereas few interaggregate pores are present in the oven-dried sample (Fig. 15*b*). A large quantity of intra-aggregate pores with radii smaller than 1 μm is present in both the saturated and oven-dried samples.

The measured PSDs of four soil samples at different degrees of saturation are shown in Fig. 16*a*. Generally speaking, the pores after the drying process are essentially intra-aggregate pores with few interaggregate pores. The pore vol-

Fig. 15. Scanning micrographs: (*a*) saturated compacted soil sample, ×1500; (*b*) oven-dried saturated compacted sample, ×3700.

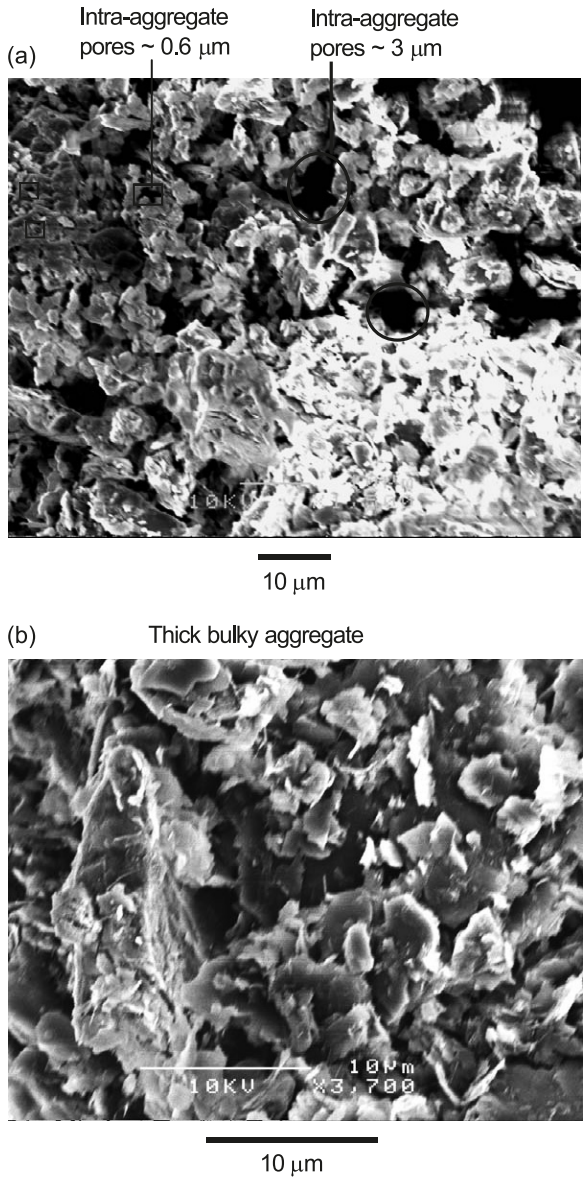

umes in 1 g of dry soil are compared in Fig. 17 with respect to pore radius. Both the volume of interaggregate pores and the volume of intra-aggregate pores decrease as the degree of saturation decreases. The total pore volume also decreases as the degree of saturation decreases, which indicates that the soil shrinks during the drying process.

As soil suction is increased to 100 kPa (S_r = 0.8, where S_r is the degree of saturation), the differential pore volume of the pores above 0.5 μm decreases when compared with the saturated soil sample. At the same time, the differential pore volume of the pores smaller than 0.5 μm is similar to the saturated soil sample. The soil sample shrinks freely during the drying process. The pores are expected to shrink due to the water meniscus progressing from larger pores to smaller pores as suction increases. Referring to eq. [1] and choosing the surface tension of water T_s at a temperature of 25 °C as 72 μm/m^2 and a contact angle of 0°, the maximum

Fig. 16. PSDs of saturated compacted samples dried to different degrees of saturation.

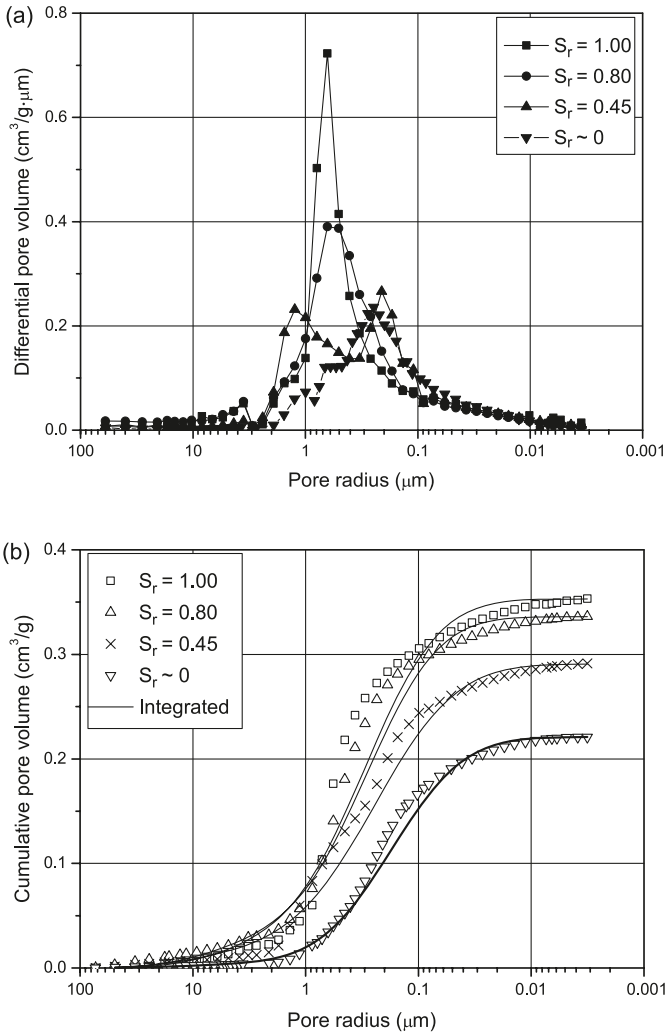

Fig. 17. Variation of volumes of interaggregate pores and intra-aggregate pores at different degrees of saturation.

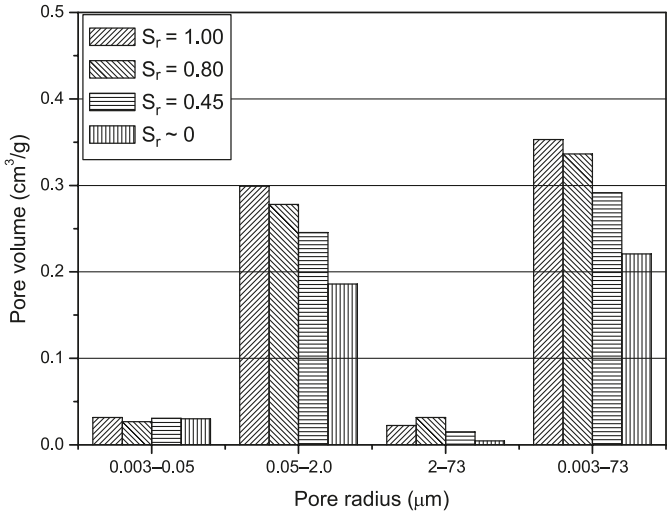

Table 4. Best-fit analysis results for PSDs of originally saturated compacted samples during drying process.

				PSD of interaggregate pores			PSD of intra-aggregate pores		
Suction (kPa)	Water content (%)	Degree of saturation	Void ratio	a_1 (cm^3/g)	μ_1	σ_1	a_2 (cm^3/g)	μ_2	σ_2
<1	37.8	1.00	1.00	0.027	0.74	0.41	0.33	–0.52	0.52
100	29.2	0.80	0.96	0.036	0.72	0.47	0.30	–0.54	0.50
500	14.2	0.45	0.84	0.021	0.86	0.50	0.27	–0.61	0.57
> 10^5	~0	~0	0.65	0.006	0.88	0.52	0.22	–0.76	0.50

pore radius filled with water at a suction of 100 kPa is 1.44 μm. As suction is increased to 100 kPa, the pores with radii larger than 1.44 μm will drain and are expected to shrink. Limited influence is expected on the pores with radii smaller than 1.44 μm as the suction is increased to 100 kPa.

As soil suction is increased to 500 kPa (S_r = 0.45), the pore densities between 0.1 and 2 μm form a trough. A decrease in differential pore volume with radii larger than 0.3 μm and an increase of differential pore volume with radii smaller than 0.3 μm were found in the sample drained from a suction of 100 to 500 kPa. As suction is increased to 500 kPa, the pores with radii larger than 0.29 μm will drain and are expected to shrink. The differential pore volumes with radii smaller than 0.29 μm will decrease. As many pores larger than 0.29 μm shrink into smaller pores, the quantity and differential pore volumes of the pores smaller than 0.29 μm will increase.

The differential pore volumes with radii larger than 0.4 μm decreased significantly after the soil sample was oven-dried (S_r ~0) when compared with the soil sample at a suction of 500 kPa (S_r = 0.45). Dineen (1997) and Cafaro (2002) discussed a noticeable void ratio decrease during soil drying and suggested that the particle system minimizes its potential energy during drying through an immediate change of the pore-size distribution taking place when suction reaches a threshold value (i.e., 1400 kPa suggested by Dineen). The observed decrease in differential pore volume with radii larger than 0.4 μm in this study may occur at the threshold suction. The pores larger than 0.4 μm may collapse at the threshold suction. The loss of water at the boundary due to evaporation may induce arching or bridges that bond the soil particles together. It should also be considered that an increase in pore water salinity may take place during drying associated with water evaporation (Cafaro 2002).

Two log-normal distributions can be combined to describe the pore-size distributions of the samples obtained during the soil drying process similar to the cases of soil compaction and saturation. The parameters obtained from the regression analysis are listed in Table 4. The measured cumulative pore-volume curves and the integrated pore-volume curves based on the fitted PSDs are shown in Fig. 16*b*.

Changes in the volume of interaggregate pores and intra-aggregate pores are equal to the total soil volume change. With the application of eq. [10], the void ratio values of the soil samples at 100 and 500 kPa suction values and the oven-dried soil sample are calculated (as shown in Table 1). Furthermore, the interaggregate pore-size distributions and the intra-aggregate pore-size distributions are related to the void ratio. Regression analyses based on the data listed in Table 4 give λ_1 = –0.46, λ_2 = 0.69, λ_3 = 0.9, λ_4 = 0.6, and k_1 = 0.75. Again, k_1 = 0.75 means that about 75% of volume change occurs in the intra-aggregate pores and only 25% of volume change occurs in the interaggregate pores for the saturated soil samples.

Conclusions

The soil microporosity structure of a lean clay with sand was studied using SEM and MIP. An unsaturated sample, a bulky soil sample, a saturated sample, and an oven-dried sample were tested using SEM to observe the microporosity structures on soil surfaces. The pore-size distributions of a series of compacted samples, saturated samples, and dried samples were measured using MIP to quantitatively characterize the characteristics and variations of soil microporosity structure during compaction, saturation, and drying. The following conclusions can be drawn based on the results of these tests:

(1) A dual-porosity structure can be represented by interaggregate pores and intra-aggregate pores formed during the compaction process. The dual-porosity structure was similar in both unsaturated compacted samples and saturated compacted samples.

(2) The change of the interaggregate pores is dominant during soil compaction and the change of the intra-aggregate pores is dominant during soil saturation and drying.

(3) The compaction compression stress can cause significant reduction in the volume of the interaggregate pores, but only slightly affects the intra-aggregate pores during compaction.

(4) The dual-porosity structure evolutes during the saturation process. During a confined saturation process, the soil aggregates may swell and result in larger and more intra-aggregate pores, but smaller and fewer interaggregate pores.

(5) During the soil drying process, the soil samples shrink to lower void ratios and the intra-aggregate pores contract to smaller radii.

(6) A mathematical model was developed to describe the bimodal PSDs and to relate the soil PSDs with void ratio. The PSD at an arbitrary void ratio subjected to different deformation histories can be predicted using the empirical parameters calibrated through the MIP tests.

Acknowledgement

This research was substantially supported by a grant from the NSFC/RGC Joint Research Scheme between the National Natural Science Foundation of China and the Re-

search Grants Council of the Hong Kong Special Administration Region (Project No. N-HKUST611/03).

References

Alonso, E.E., Gens, A., and Hight, D.W, 1987. Special problem soils. *In* Proceedings of the 9th European Conference on Soil Mechanics and Foundation Engineering, Dublin, Ireland, 31 August – 3 September 1987. *Edited by* E.T. Hanrahan, T.L.L. Orr, and T.F. Widdis. A.A. Balkema, Rotterdam, the Netherlands. pp. 1087–1146.

Anandarajah, A., and Lavoie, D. 2002. Numerical simulation of the microstructure and compression behavior of Eckernforde Bay sediments. Marine Geology, **182**: 3–27.

ASTM. 2000. Standard practice for classification of soils for engineering purposes (Unified Soil Classification System). ASTM standard D2487. 2000 Annual Book of ASTM Standards. American Society for Testing and Materials (ASTM), Philadelphia, Pa.

Barden, L., and Sides, G. 1970. Engineering behavior and structure of compacted clays. Journal of Soil Mechanics and Foundation Analysis, **96**: 1171–1200.

Basma, A.A., Al-Homoud, A.S., Husein, M., and Ai-Bashabsheh, M.A. 1996. Swelling-shrinkage behavior of natural expansive clays. Applied Clay Science, **11**(2–4): 211–277. doi:10.1016/S0169-1317(96)00009-9.

BSI. 1990. Methods of test for soils for civil engineering purposes. Compaction-related tests. Standard BS 1377-4:1990. British Standards Institution (BSI), London.

Cafaro, F. 2002. Metastable states of silty clays during drying. Canadian Geotechnical Journal, **39**(4): 992–999. doi:10.1139/t02-039.

Coulon, E., and Bruand, A. 1989. Effects of compaction on the pore space geometry in sandy soils. Soil and Tillage Research, **15**(1–2): 137–152. doi:10.1016/0167-1987(89)90070-6.

Cuisinier, S., and Laloui, L. 2004. Fabric evolution during hydromechanical loading of a compacted silt. International Journal for Numerical and Analytical Methods in Geomechanics, **28**(6): 483–499. doi:10.1002/nag.348.

Delage, P., and Lefebvre, G. 1984. Study of the structure of a sensitive Champlain clay and of its evolution during consolidation. Canadian Geotechnical Journal, **21**(1): 21–35. doi:10.1139/T84-003.

Dineen, K. 1997. The influence of soil suction on compressibility and swelling. Ph.D. thesis, University of London, London.

Fredlund, M.D., Fredlund, D.G., and Wilson, G.W. 2000. An equation to represent grain-size distribution. Canadian Geotechnical Journal, **37**(4): 817–827. doi:10.1139/cgj-37-4-817.

Fredlund, M.D., Wilson, G.W., and Fredlund, D.G. 2002. Use of grain-size distribution for the estimation of the soil-water characteristic curve. Canadian Geotechnical Journal, **39**(5): 1103–1117. doi:10.1139/t02-049.

Griffiths, F., and Joshi, R. 1989. Change in pore-size distribution due to consolidation of clays. Géotechnique, **39**(1): 159–167.

Lennart, R., and Bertil, W. 2004. Mathematics handbook for science and engineering. 5th ed., Springer, New York.

Mallants, D., Mohanty, P., Vervoort, A., and Feyen, J. 1997. Spatial analysis of saturated hydraulic conductivity in a soil with macropores. Soil Technology, **10**(2): 115–131. doi:10.1016/S0933-3630(96)00093-1.

Penumadu, D., and Dean, J. 2000. Compressibility effect in evaluating the pore-size distribution of kaolin clay using mercury intrusion porosimetry. Canadian Geotechnical Journal, **37**(2): 393–405. doi:10.1139/cgj-37-2-393.

Pruess, K., Wang, J.S.Y., and Tsang, Y.W. 1990. On thermohydrologic conditions near high-level nuclear wastes emplaced in partially saturated fractured tuff. 2. Effective continuum approximation. Water Resources Research, **26**(6): 1249–1261.

Rao, S.M., and Revanasiddappa, K. 2005. Role of microfabric in matrix suction of residual soils. Engineering Geology, **80**(1–2): 60–70. doi:10.1016/j.enggeo.2005.04.001.

Simms, P., and Yanful, E. 2001. Measurement and estimation of pore shrinkage and pore distribution in a clayey till during soil-water characteristic curve tests. Canadian Geotechnical Journal, **38**(4): 741–754. doi:10.1139/cgj-38-4-741.

Sivakumar, V., and Wheeler, S. 2000. Influence of compaction procedure on the mechanical behaviour of an unsaturated compacted clay. Part 1: Wetting and isotropic compression. Géotechnique, **50**(4): 359–368.

Sridharan, A., Altaschaeffl, A.G., and Diamond, S. 1971. Pore-size distribution studies. Journal of the Soil Mechanics and Foundations Division, **97**(5): 771–787.

Zhang, L.M., and Fredlund, D.G. 2003. Characteristics of water retention curves for unsaturated fractured rocks. *In* Proceedings of the 2nd Asian Conference on Unsaturated Soils, Osaka, Japan, 15–17 April 2003. *Edited by* D. Karube, A. Iizuka, S. Kato, K. Kawai, and K. Tateyama. pp. 425–428.

Zhao, J.J., Wang, S.J., Shang, Y.J., and Yue, Z.Q. 2005. Consolidation characteristics of completely decomposed granite in Hong Kong. Journal of Hohai University (Natural Sciences), **33**(1): 85–88. [In Chinese.]